A radar package for asteroid subsurface investigations: Implications of implementing and integration into the MASCOT nanoscale landing platform from science requirements to baseline design

Alain Hérique, Dirk Plettemeier, Caroline Lange, Jan Thimo Grundmann, Valérie Ciarletti, Tra-Mi Ho, Wlodek Kofman, Benoit Agnus, Jun Du, Wenzhe Fa, et al.

Accepted Manuscript

A radar package for asteroid subsurface investigations: Implications of implementing and integration into the MASCOT nanoscale landing platform from science requirements to baseline design

Alain Herique, Dirk Plettemeier, Caroline Lange, Jan Thimo Grundmann, Valerie Ciarletti, Tra-Mi Ho, Wlodek Kofman, Benoit Agnus, Jun Du, Wenzhe Fa, Oriane Gassot, Ricardo Granados-Alfaro, Jerzy Grygorczuk, Ronny Hahnel, Christophe Hoarau, Martin Laabs, Christophe Le Gac, Marco Mütze, Sylvain Rochat, Yves Rogez, Marta Tokarz, Petr Schaffer, André-Jean Vieau, Jens Biele, Christopher Buck, Jesus Gil Fernandez, Christian Krause, Raquel Rodriguez Suquet, Stephan Ulamec

Please cite this article as: A. Herique, D. Plettemeier, C. Lange, J.T. Grundmann, V. Ciarletti, T.-M. Ho, W. Kofman, B. Agnus, J. Du, W. Fa, O. Gassot, R. Granados-Alfaro, J. Grygorczuk, R. Hahnel, C. Hoarau, M. Laabs, C. Le Gac, M. Mütze, S. Rochat, Y. Rogez, M. Tokarz, P. Schaffer, André.-Jean. Vieau, J. Biele, C. Buck, J. Gil Fernandez, C. Krause, R.R. Suquet, S. Ulamec, A radar package for asteroid subsurface investigations: Implications of implementing and integration into the MASCOT nanoscale landing platform from science requirements to baseline design, *Acta Astronautica* (2018), doi: 10.1016/j.actaastro.2018.03.058.

A RADAR PACKAGE FOR ASTEROID SUBSURFACE INVESTIGATIONS: IMPLICATIONS OF IMPLEMENTING AND INTEGRATION INTO THE MASCOT NANOSCALE LANDING PLATFORM FROM SCIENCE REQUIREMENTS TO BASELINE DESIGN

Alain Herique[(1)], **Dirk Plettemeier**[(2)], **Caroline Lange**[(3)], **Jan Thimo Grundmann**[(3)], **Valerie Ciarletti**[(4)], **Tra-Mi Ho**[(3)], **Wlodek Kofman**[(1,5)], **Benoit Agnus**[(4)], **Jun Du**[(5)], **Wenzhe Fa**[(5)], **Oriane Gassot**[(1)], **Ricardo Granados-Alfaro**[(1)], **Jerzy Grygorczuk**[(6)], **Ronny Hahnel**[(2)], **Christophe Hoarau**[(8)], **Martin Laabs**[(2)], **Christophe Le Gac**[(4)], **Marco Mütze**[(2)(4)], **Sylvain Rochat**[(1)], **Yves Rogez**[(1)], **Marta Tokarz**[(7)], **Petr Schaffer**[(2)], **André-Jean Vieau**[(4)], **Jens Biele**[(9)], **Christopher Buck**[(10)], **Jesus Gil Fernandez**[(10)], **Christian Krause**[(9)], **Raquel Rodriguez Suquet**[(11)], **Stephan Ulamec**[(9)]

[(1)] *Univ. Grenoble Alpes, CNRS, IPAG, F-38000 Grenoble, France*
[(2)] *Technische Universität Dresden, 01069 Dresden, Germany*
[(3)] *DLR German Aerospace Center, Institute of Space Systems, Robert-Hooke-Strasse 7, 28359 Bremen, Germany*
[(4)] *LATMOS/IPSL, UVSQ Université Paris-Saclay, UPMC Univ. Paris 06, CNRS, Guyancourt, France*
[(5)] *Space Research Centre of Polish Academy of Sciences, Bartycka 18A, 00-716 Warsaw, Poland*
[(6)] *IRSGIS, Peking University, Beijing, China*
[(7)] *ASTRONIKA Sp. Z o.o., 00-716 Warszawa, Poland*
[(8)] *CNRS, Néel Institut, 38000 Grenoble, France*
[(9)] *DLR German Aerospace Center, Space Operations and Astronaut Training – MUSC, 51147 Köln, Germany*
[(10)] *ESA, ESTEC, 2200 AG, Noordwijk, The Netherlands*
[(11)] *CNES, F-3100, Toulouse, France*

Abstract

The internal structure of asteroids is still poorly known and has never been analyzed directly by measurements. Our knowledge relies entirely on inferences from remote sensing observations of the surface and theoretical modeling. Direct measurements are crucial to characterize an asteroid's internal structure and heterogeneity from sub-metric to global scale. The radar package developed in the frame of the phase A/B1 of the Asteroid Impact Mission (AIM) as part of the larger Asteroid Impact & Deflection Assessment (AIDA) mission is a mature instrument suite to answer this question and to improve our ability to understand and model the mechanisms driving Near Earth Asteroids (NEA). It is of main interest for science, exploration and planetary defense. This instrument suite consists of a monostatic high frequency radar (HFR) to investigate the stratigraphy of surface regolith and a bistatic low frequency radar (LFR) to characterize the deep interior. The chosen platform to deliver the surface unit of the LFR and other instruments for a close-up study of the target asteroid is the MASCOT nanolander, which already flies on Hayabusa2 (HY2) in a mineralogy scout configuration. In this paper, we present the chosen instrumentation for radar science, baseline mission requirements and the initial design for integration into the lander platform, including all peculiarities and constraints.

1. Introduction

The observations of asteroid-like bodies and especially their internal structure are of main interest for science as well as planetary defense. Despite some highly successful space missions to Near-Earth Objects (NEOs), their internal structure remains largely unknown [1-3]. There is some evidence that an aggregate structure covered by regolith ("rubble pile") is very common for medium size bodies, but there are no direct observations. The size distribution of the constitutive blocks is unknown: is it fine dust, sand, pebbles, larger blocks, or a mixture of all of these? Observations of asteroid-like bodies hint at the existence of a whole range of variation between these very extreme objects. Some may be 'fluffballs' composed entirely of highly porous fine-grained material [4]. There are also very large objects that appear to be at least somewhat cohesive [5], and possibly monoliths bare of any regolith layer [6]. Binary systems in their formation by evolution of asteroid spin state [7] appear to disperse, re-aggregate or reconfigure their constitutive blocks over time [8], leading to a complex geological structure and history [9-11]. This history includes components of separated binaries appearing as single bodies [12,13] as well as transitional states of the system including highly elongated objects [14], contact binaries [15-17] and possibly ring systems [18]. The observed spatial variability of the regolith is not fully explained and the mechanical behavior of granular materials in a low gravity environment remains difficult to model.

After several asteroid orbiting missions, these crucial and yet basic questions remain open. Direct measurements are mandatory to answer these questions. Therefore, the modeling of the regolith structure and its mechanical reaction is crucial for any interaction of a spacecraft with a NEO, particularly for a deflection mission. Knowledge about the regolith's vertical structure is needed to model thermal behavior and thus Yarkovsky (cf. [19,20]) and YORP accelerations. Determination of the global structure is a way to test stability conditions and evolution scenarios. There is no way to determine this from ground-based observations (see [1] for a detailed review of the science rationale and measurement requirements).

2. Radar Sounding of Asteroids

A radar operating remotely from a spacecraft is the most mature instrument capable of achieving the science objective to characterize the internal structure and heterogeneity of an asteroid, from sub-metric to global scale, for the benefit of science as well as planetary defense, exploration and in-situ resource prospection [1,20,21]. As part of the payload of the AIM mission a radar package was proposed to the ESA Member States during the Ministerial council meeting in 2016 [10,22]. In the frame of the joint AIDA demonstration mission, DART (Double Asteroid Redirection Test) [11], a kinetic impactor, was designed to impact on the moon of the binary system, (65803) Didymos, while ESA's AIM [10] was designed to determine the momentum transfer efficiency of the kinetic impact and to observe the target structure and dynamic state.

Radar capability and performance is mainly determined by the choice of frequency and bandwidth of the transmitted radio signal. Penetration depth increases with decreasing frequency due to lower attenuation. Resolution increases with bandwidth. Bandwidth is necessarily lower than the highest frequency, and antenna size

constraints usually limit the lowest frequency. These are the main trade-off factors for instrument specification, which also has to take into account technical constraints such as antenna accommodation or operation scenarios [1].

The AIM mission would have had two complementary radars on board, operating at different frequencies in order to meet the different scientific objectives [1]. A monostatic radar operating at higher frequencies (HFR) can achieve the characterization of the first ten meters of the subsurface with a metric resolution to identify layering and to link surface measurements to the internal structure. Deep interior structure tomography requires a low frequency radar (LFR) in order to propagate through the entire body and to characterize the deep interior. The HFR design is based on the WISDOM radar [23,24] developed for the ExoMars / ESA-Roskosmos mission and LFR is a direct heritage of the CONSERT radar designed for ESA's Rosetta mission.

3. HFR: High Frequency Radar for Regolith Tomography

The monostatic HFR radar on board the orbiter spacecraft is a high frequency synthetic aperture radar (SAR) to perform reflection tomography of the first tens of meters of the regolith with a metric resolution [1]. It can image the shallow subsurface layering and connect the surface measurements to the internal structure. The HFR is a stepped frequency radar operating from 300 MHz to 800 MHz in nominal mode and up to 3 GHz in an optional mode. It inherits from the WISDOM radar and is optimized to study small bodies.

Table 1 summarizes the main characteristics and budgets of the radar. It provides a decimetric vertical resolution and better than one meter resolution in horizontal direction, depending on the spacecraft speed relative to the asteroid surface. This high resolution allows characterizing the spatial variation of the regolith texture, which is related to the size and mineralogy of the constituting grains and macroporosity.

A primary objective of the HFR within the AIM mission was the characterization of the regolith of Didymoon, the Didymos system's secondary body or moon of the primary, Didymain.The HFR was supposed to survey Didymoon before and after the DART impact, in order to determine the structure and layering of the secondary's shallow subsurface down to a few meters. The tomography of the DART artificial impact crater would further provide a better estimate of the ejected mass to model the momentum transfer efficiency.

Table 1: Main characteristics and performance
of the bistatic low frequency radar and the monostatic high frequency radar.

	Bistatic Radar		Monostatic Radar
	Orbiter	Lander	
Frequency (nominal)	50-70 MHz		300 – 800 MHz
Frequency (extended)	45-75 MHz		up to 3 GHz
Signal modulation	BPSK		Step frequency
Resolution	10 – 15 m (1D)		1 m (3D)
Polarization	Circular (AIM)	Linear (Mascot)	Tx: 1 Circular
			Rx: OC and SC
Tx power	12 W		20 W
Pulse repetition	5 seconds		1 second (typical)
Sensitivity	Dynamic = 180 dB		NEσ0 = -40 dB.m^2/m^2
Mass			
Electronic	920 g	920 g	830 g
Antenna	470 g	230 + 100 g	1560 g
Total w/o margin	1390 g	1250 g	2390 g
Power max / mean	50 W / 10 W	50 W / 10 W	137 W / 90 W
Typical Data (Gbit)	1	0.3	300

With a single acquisition sequence, Didymoon mapping provides the 2D distribution of geomorphological elements (rocks, boulders, etc.) that are embedded in the subsurface. Multipass acquisition and processing is required to obtain the 3D tomography of the regolith. Another primary objective is the determination of the dielectric properties of the subsurface of Didymoon. The dielectric permittivity can be derived from the spatial signature of individual reflectors or by analyzing the amplitude of the surface echoes.

3.1. Instrument Design

The HFR electronics (Figure 2) uses a heterodyne system architecture utilizing two frequency generators to form a stepped frequency synthesizer. Transmitted wave as well as the local oscillator frequencies are generated separately and incoherently with phase-locked loop (PLL) synthesizers. A functional block schematic of the radar system shows Figure 1. Its front-end mainly consists of a high output power transmitter and two dedicated receivers. The antenna is fed by a 0° and a 90° phase shifted signal to generate circular polarization for the transmitted wave, using a 90° hybrid divider. The transmitter output is muted during reception by switching off the power amplifier output, in order to not overload the receivers. A separate receiver processes one of the receive polarization respectively. For the SAR operation mode an ultra-stable frequency reference provides a stable reference to the digital and RF electronics. All modules are supplied by a dedicated DC/DC module, which provides all necessary supply voltages for the individual blocks from a single primary input voltage.

The receiver's superheterodyne architecture uses a medium intermediate frequency at the digitizer input. This ensures high performance by eliminating the 1/f noise, thereby improving noise and interference performance. A calibration subsystem allows for a calibration of the horizontal (H) and vertical (V) receiver regarding image rejection, inter-receiver phase and amplitude balance. The received H- and V-signals are compensated subsequently to ensure very high polarization purity.

The Digital Module (DM) is built around a Field Programmable Gate Array (FPGA) and microcontroller. It controls and manages the data flow of the instrument. This includes digital signal processing of the measurement data, short time data accumulation, transfer to the spacecraft and processing of control commands for radar operation.

The antenna system comprises of a single antenna, which transmits circular polarization and receives both linear polarizations. This ultra-wideband dual-polarized antenna system operates in the frequency range from 300 MHz to 3.0 GHz. Figure 3 shows a 3D model and its corresponding antenna prototype. Antenna diagrams are shown in Figure 4. The antenna consists of two orthogonally crossed antenna blades and is fed by two signals with a phase difference of 90°. In this configuration, it is possible to receive circular polarized electromagnetic signals even if only linear polarization is required. This antenna system, in conjunction with the separate receivers, allows a fully polarimetric acquisition and generation of virtual circular receive polarizations after digital processing.
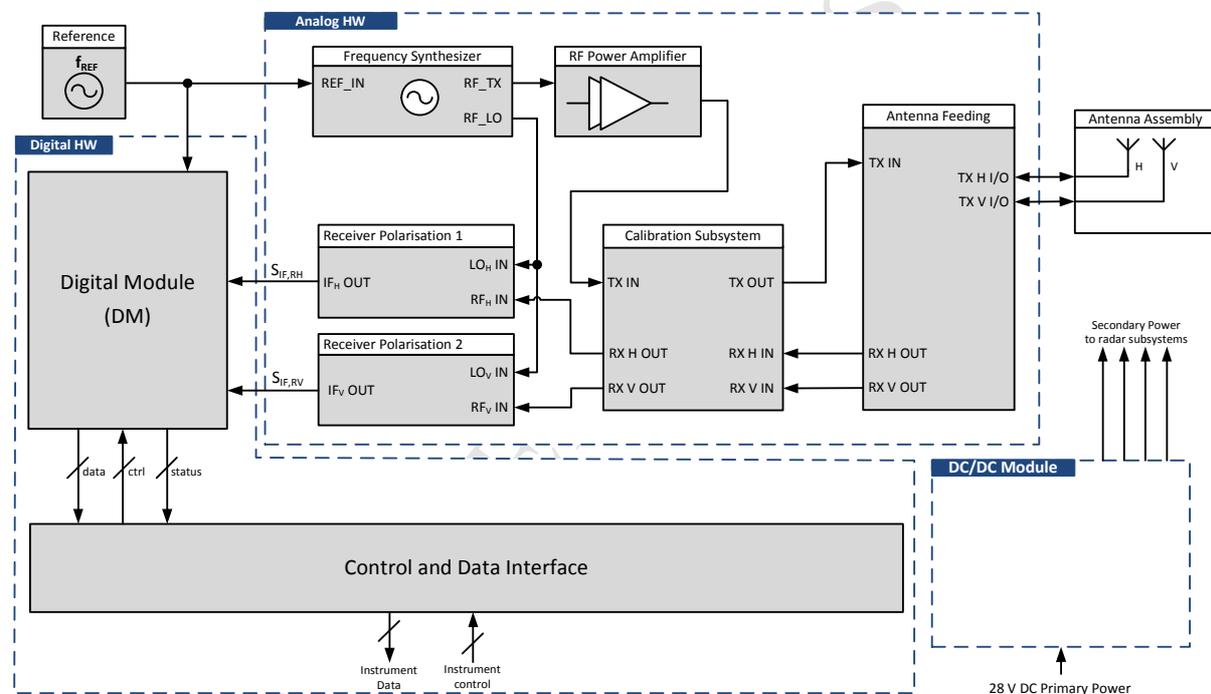

Figure 1: Functional block schematic of the HFR radar system showing the main blocks including reference source, frequency synthesizer, RF power amplifier, calibration subsystem, antenna feeding, antenna assembly, receiver channels and digital module.
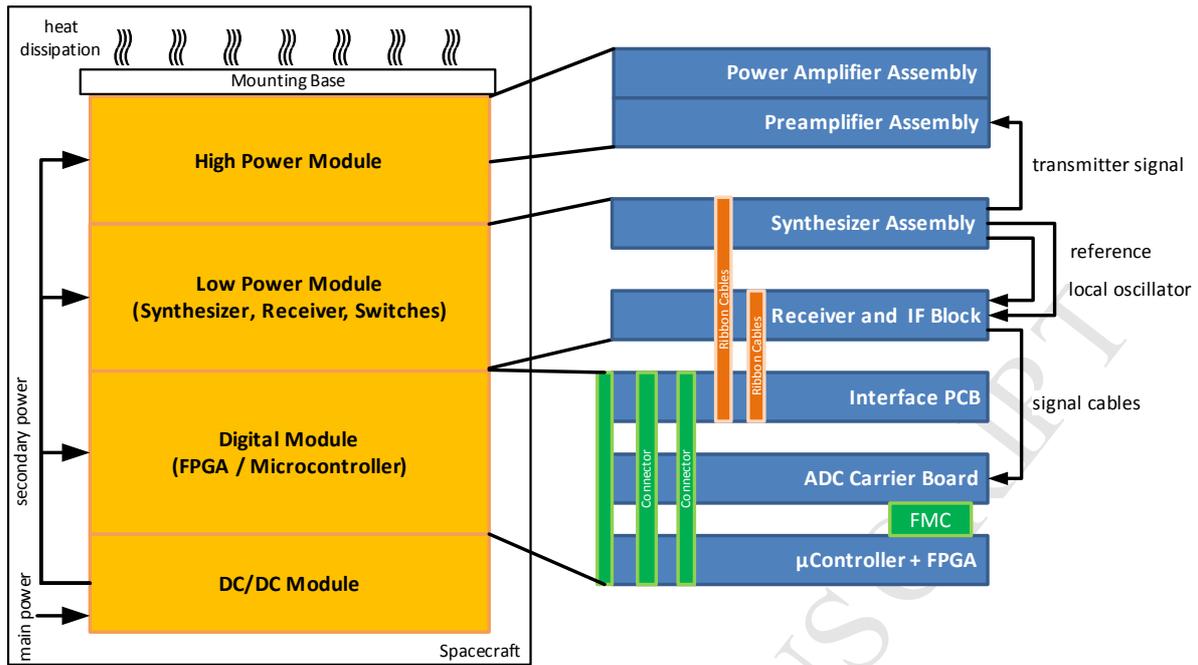
Figure 2: Module stack of the HFR system prototype: DC/DC Module, Digital Module with FPGA, microcontroller and signal level converters, Low Power Module with synthesizer, receiver and switches for calibration, and High Power Module with power amplifier and preamplifier assemblies.

Figure 3: 3D model (left) and prototype (right) of the HFR ultra-broadband dual polarized antenna.
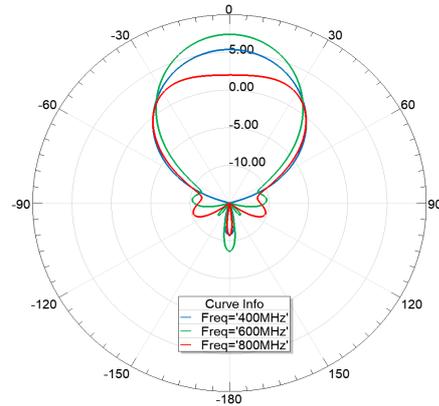
Figure 4: Simulated antenna pattern of HFR antenna system (E-plane).

3.2. Operations and Operational Constraints

The requirements for the HFR instrument are strongly driven by the acquisition geometry. Indeed, Synthetic Aperture Radar reflection tomography in 3D requires observations of different geometries and can only be achieved by constraining the spacecraft motion and position with respect to the observed target. For each acquisition geometry, the radar acquires the signal returned by the asteroid as function of propagation time, which is a measure of the distance from the spacecraft to the observed body. This range measurement resolves information in a first spatial dimension. The resolution in that dimension is given by the bandwidth of the radar signal and is significantly better than one meter (~30 cm in vacuum).

For kilometric-size asteroids, the rotational period is generally in the order of a few hours, much smaller than the spacecraft orbital period during remote observation operations within the Hill sphere. In the Didymos system, the main body's rotation period is 2.3 h. Its moon orbits the primary in 11.9 h and it is expected to rotate synchronously [10]. The spacecraft's orbital period in a gravitationally bound orbit of 10 km radius is nearly two weeks. It can also be at rest relative to the system's barycenter while on a heliocentric station-keeping trajectory.

For the processing, we consider the body fixed frame with a spacecraft moving in the asteroid sky (Figure 7). Thus, the relative motion along the orbit plane between the spacecraft and the moon resolves a second dimension by coherent Doppler processing (Figure 5) [25]. This brute-force SAR processing takes into account the observation geometry to give 2D images of the body surface mixing in the same pixel surface and subsurface features (Figure 5c). For a spherical body this induces an ambiguity between North and South hemispheres [26] which corresponds to the aliasing of the North target to the South hemisphere in Figure 5a.
Therefore, the resolution is determined by the length of the observation orbit arc (i.e., Doppler bandwidth) and is better than one meter for an arc of 20° longitude. For the Didymos system, the surfaces of the primary and secondary object show very different Doppler behavior due to their different periods of rotation. This allows to resolve ambiguities when both are inside the radar's field of view.
In addition, a spacecraft position out of the equatorial plane breaks the symmetry. Shifting the signal partially out of the orbital plane reduces the North to South ambiguities as it is spread and a less powerful alias remains in the other hemisphere (South in Figure 5a). The accuracy requirement for the spacecraft pointing is typically 5° when the reconstructed trajectory accuracy requirement is in the order of hundreds of meters. The orbit restitution accuracy can be improved by the SAR processing itself using autofocus techniques [27].

To achieve a 3D tomography, the third dimension to be resolved needs to be orthogonal to the orbit plane (Figure 7). To do so, the HFR instrument performs several passes at different latitudes. Typically, 20 passes allow a metric resolution. The spacecraft position evolves in a declination and right ascension window centered around 30° radar incidence of the observed target point (Figure 7). The extent of this window is about 20°. Each pass lasts for one to two hours and is traversed close to constant declination. The spacecraft is in very slow motion of a few mm/s along this axis orthogonal to the orbit plane. Such a velocity is difficult to achieve in operations. A proposed solution is to combine this slow motion to a movement along the orbit axis. All the passes can be done in a single spacecraft trajectory. Each pass corresponds to the period when HFR is facing the moon that is orbiting around the main body (Figure 7). In this multi-pass scenario, the resulting resolution for the third direction is 1 m and it is the limiting one (Figure 6).

The distance between the HFR instrument and its target is limited by the radar link budget for the upper boundary and by the speed of the electronic system for the lower boundary. HFR is expected to operate from 1 km up to 35 km, the nominal distance being 10 km.

(a)

(b)

(c)
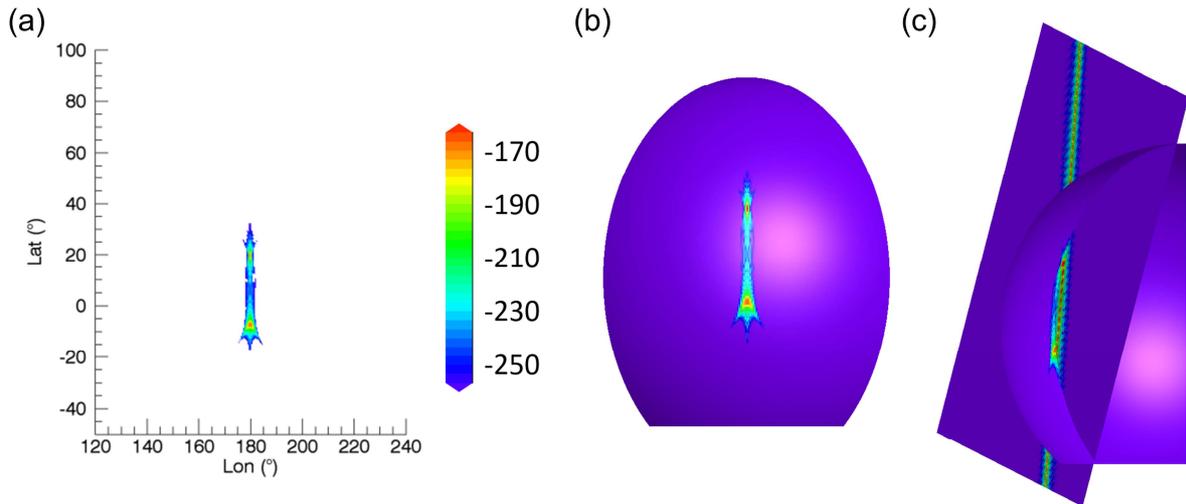
Figure 5: HFR mono pass impulse response on Didymoon's surface map for a point target located at 20° latitude and 180° longitude (a). The impulse response power is shown by color mapping, in dB. The same impulse response presented in 3D on a sphere portion that represents the surface of Didymoon (b) and shown in 3D (c). Note that a clear ambiguity along the vertical axis remains in a mono pass. The color scale corresponds to a dynamic range of 100 dB and exaggerates signal distortions. This measurement is simulated, along an arc of orbit or 20°, considering an isotropic point target located. On Didymoon's surface and taking into account propagation delay and geometrical losses. Simulation was done in the frequency domain using the instrument characteristics listed in this paper. A SAR processor, corresponding to a coherent summation after compensation of the propagation delay, processes the simulated measurements.

(a)

(b)

(c)
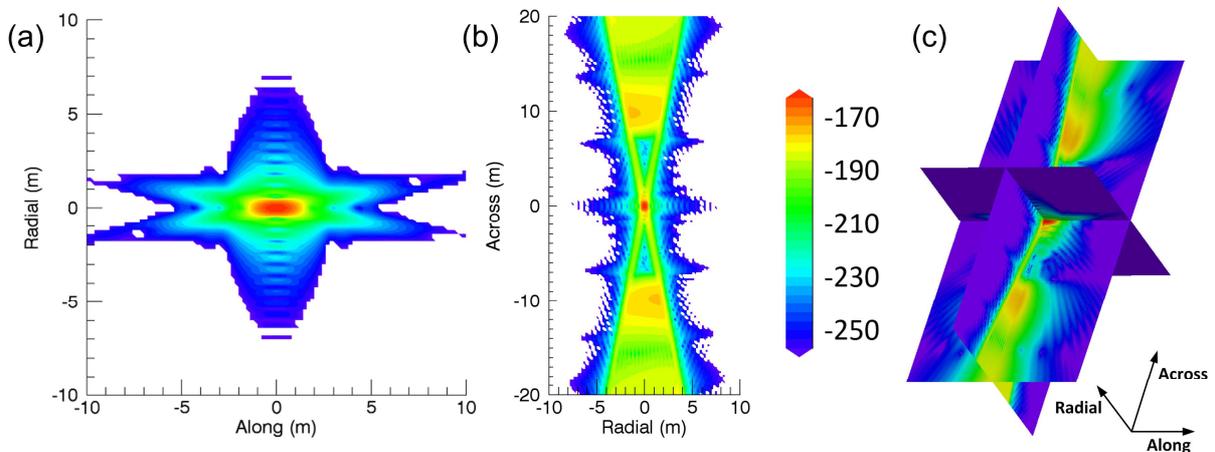
Figure 6: HFR impulse response with 30 passes for a point target located on Didymoon's surface at 30° latitude and 90° longitude. The HFR observation window is chosen so that it has a 30° incidence angle with the target. The color mapping, in dB, shows the impulse response power; (a) presents a view of the radial/along track plane while (b) presents a view of the radial/across track plane; (c) presents the same impulse response planes in 3D, including the tangent plane (across/along track). The color scale corresponds to a dynamic range of 100 dB. This dynamics exaggerates signal distortions.

8
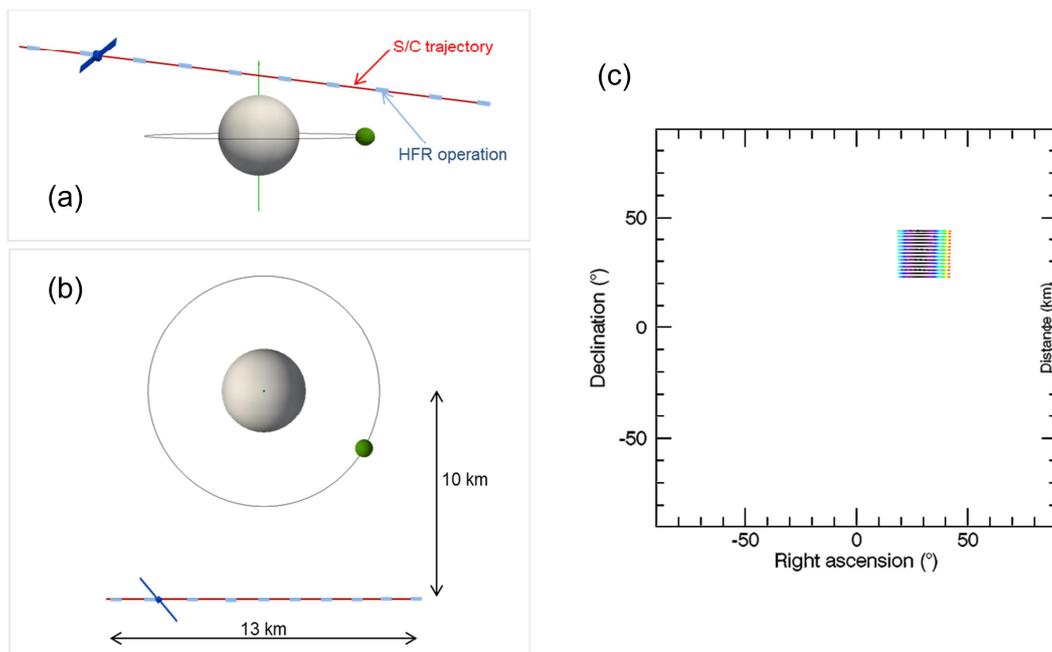
Figure 7: A typical operation scenario geometry for HFR in equatorial (a) and top view (b) in the Galilean referential frame, and the resulting acquisition window in the Didymoon's sky map (c). The arc of orbit in red correspond to 5 days of operations with an observation slot at every revolution of Didymoon.

4. LFR: Low Frequency Radar for Deep Interior Sounding

Deep interior structure tomography requires a low frequency radar to propagate through the entire body. The radar wave propagation delay and the received power are related to the complex dielectric permittivity (i.e. composition and microporosity) and the small-scale heterogeneities (scattering losses), while the spatial variation of the signal and multiple propagation paths provide information on the presence of heterogeneities (variations in composition or porosity), layers, large voids or ice lenses. A partial coverage will provide 2D cross-sections of the body; a dense coverage will allow a complete 3D tomography. Two instrument concepts can be considered (Figure 8). A monostatic radar like MARSIS/Mars Express (ESA) [28] analyzing radar waves transmitted and received by the orbiter after reflection at the asteroids' surface and internal structure or a bistatic radar like CONSERT/Rosetta (ESA) [29] analyzing radar waves transmitted by a lander, propagated through the entire body and received by the orbiter. The monostatic radar sounder requires very low operation frequencies, necessitating the use of large antennas. It is also more demanding in terms of mission resources (mass, data flow, power), driving all the mission specifications. In contrast to the monostatic approach, a bistatic radar can use slightly higher frequencies, simplifying the accommodation on the carrier mission as well as on the surface package.

9
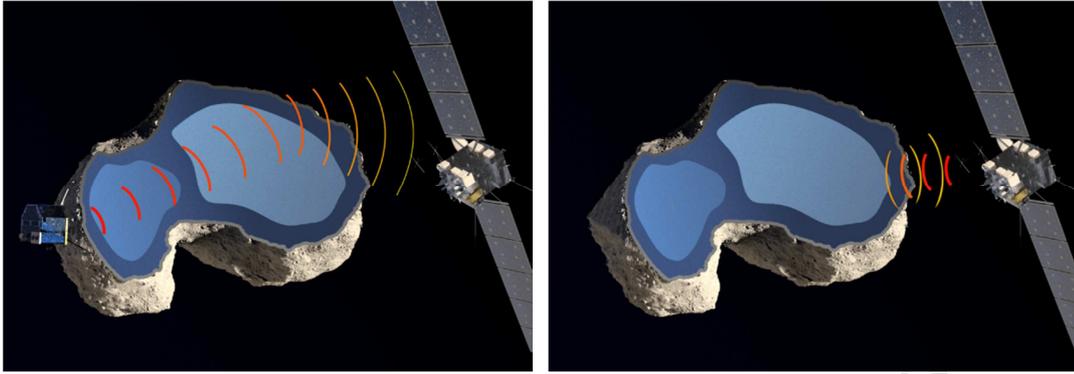
Figure 8: Bistatic (left) and monostatic (right) radar configuration, Artist view from CONSERT/Rosetta. From [1]. Credit: CGI/Rémy Rogez; shape model: Mattias Malmer CC BY SA 3.0, Image source: ESA/Rosetta/NAVCAM, ESA/Rosetta/MPS.

The bistatic low frequency radar measures the wave propagation between the surface element and an orbiter through the target object, like Didymoon. It provides knowledge of the deep structure of the moon, a key information needed to be able to model binary formation and stability conditions. The objective is to discriminate monolithic structures from building blocks, to derive the possible presence of various constituting blocks and to provide an estimate of the average complex dielectric permittivity. This information relates to the mineralogy and porosity of the constituting material. Assuming a full 3D coverage of the body, the radar determines 3D structures such as deep layering, spatial variability of the density, of the block size distribution and of the permittivity. As a beacon on the surface of Didymoon, it supports the determination of the binary system's dynamic state and its evolution induced by the DART impact (a similar approach as used for the localization of the Philae lander during the Rosetta mission [30]).

4.1. Instrument Design

The LFR radar consists of an electronic box (E-Box) shown in Figure 13 and an antenna set on each spacecraft (i.e. lander and orbiter). Both electronic units are similar: two automats sending and receiving a BPSK code modulated at 60 MHz in time-sharing (Figure 9 and Figure 14). This coded low frequency radar is an in-time transponder inherited from CONSERT on board Rosetta (ESA) [29]: in order to measure accurately the propagation delay, a first propagation path from the orbiter to the lander is processed on-board the lander. The detected peak is used to resynchronize the lander to the orbiter. A second propagation from the lander to the orbiter constitutes then in itself the science measurement (Figure 10). This concept developed for CONSERT on board Rosetta [29] allows measuring the propagation delay with a raw accuracy better than 100 ns over a few tens of hours of acquisition using a quartz oscillator with a frequency stability in the range of 10^{-7}. This accuracy can be increased up to 20 ns by on-ground processing post-processing [31], yielding a typical accuracy better than a few percent of the average dielectric permittivity. The LFR characteristics and budgets are summarized in Table 1.

10
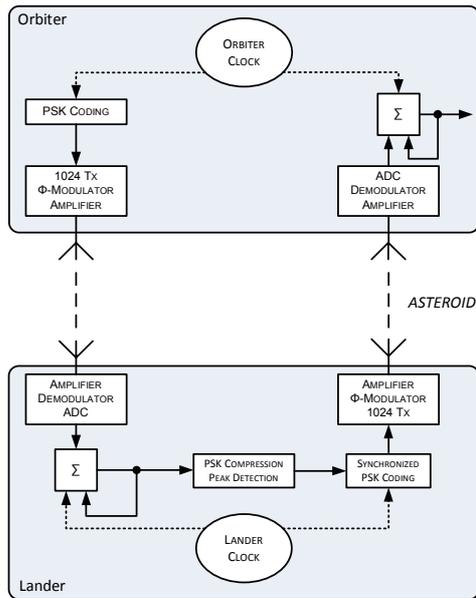
Figure 9: Block diagram of the LFR instrument, orbiter (top), lander (bottom).

.
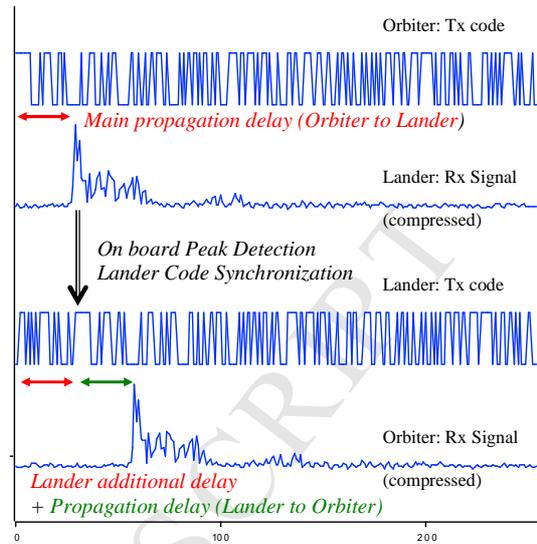
Figure 10: Lander synchronization: effect on the measured signal taking into account the periodicity of the calculated signal.
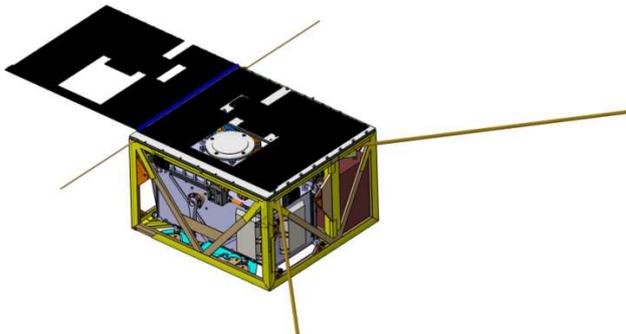
Figure 11: Lander antennas: V-shaped dipole and secondary dipole antenna. MASCOT2 accommodation.
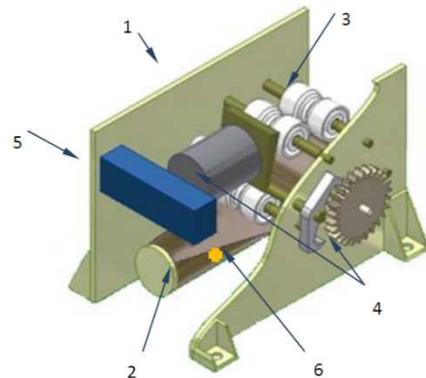
Figure 12: Antenna in tubular boom technology general architecture with basic subassemblies: (1) Structure (2) Tubular boom (3) Tubular boom guidance system (4) Drive and damping unit (5) Lock an release mechanism (6) Electrical connection.
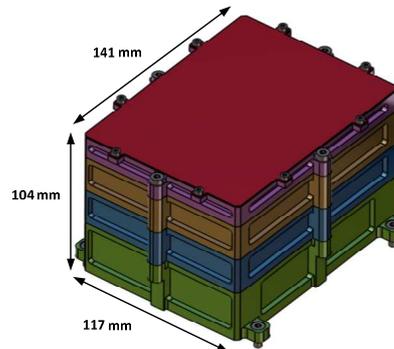
Figure 13: LFR electronic box - housing, global view.

11
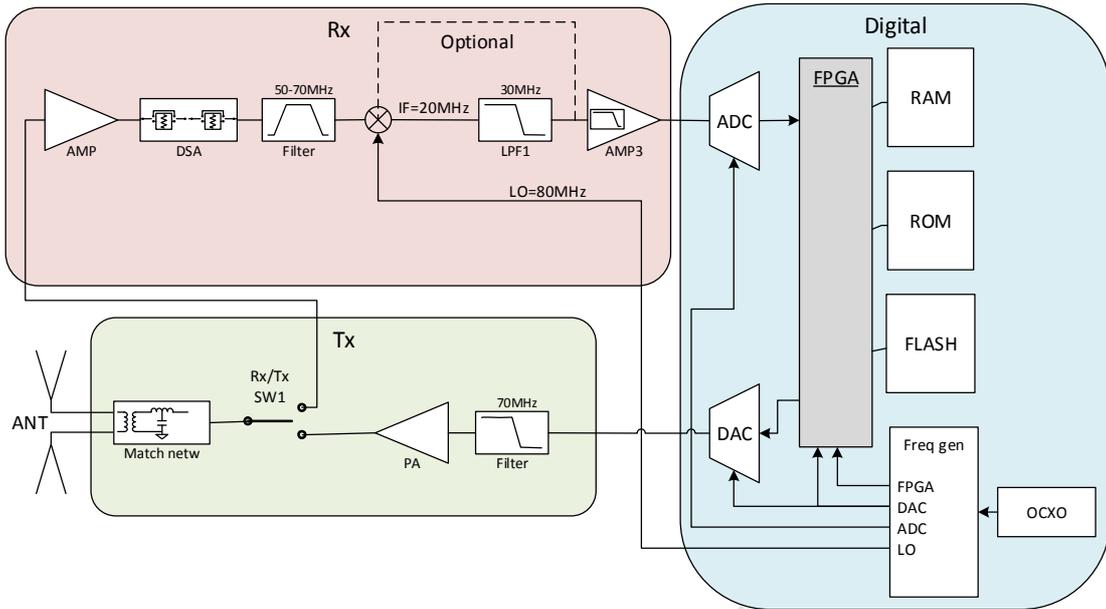
Figure 14: Block schematic of the LFR system architecture showing electronic box including transmitter (Tx), Receiver (Rx) and digital module.

As the LFR antennas cannot be deployed immediately after separation from the carrier spacecraft due to the need to relocate from the landing area to the LFR operating area, an antenna deployment mechanism is required, which needs to be operable in the low gravity environment on the surface of Didymoon. Astronika has designed a mechanical system deploying a tubular boom with a total mass of ~0.25 kg. It is able to deploy the 1.4 m antennas consuming only ~2 W for ~1 minute.

On the lander, the main antenna (V shape in Figure 11 and Figure 12) is deployed after reaching its final location. It provides linear polarization with high efficiency for the sounding through the body. A secondary antenna set with lower efficiency is deployed just after lander separation to allow operations in visibility during descent and lander rebounds, and for secondary objectives and operational purposes. The use of circular versus linear polarization induces limited power losses but reduces operational constraints on the spacecraft attitude. The LFR antenna on the orbiter is composed of four booms at the spacecraft corners in order to provide circular polarization.

4.2. Operations and Operational Constraints

Tomographic sections in bistatic mode are created in the plane of the moving line of sight *through* the target object between the lander and the orbiter passing by *underneath*. A full volume tomography is then assembled from a succession of several (as many as feasible) different of such pass geometries adjusted by changes in the orbiter trajectory. Considering the rugged topography of asteroids and the fact that all sections of the target object converge at the lander location, it is advantageous to have multiple landers and/or lander mobility, in order to ensure full volume coverage and uniform resolution of the target's interior. Lander mobility is particularly useful in binary systems where the lines of sight as well as the lander release, descent, landing, and orbiter pass trajectories can be constrained by the two

12

objects and their orbital motions relative to the spacecraft. The complex shapes and gravity fields of contact binaries or extremely elongated objects can create similar constraints.

The geometric constraints on the operational scenario for the bistatic experiment are driven by scientific and technical requirements on both the orbiter and lander platform. Considering simultaneously the baseline mission science data volume, the orbiter minimum mission duration in the frame of the AIDA mission, and the worst-case power constraints on-board of the lander, it is not possible to ensure full coverage of Didymoon according to the Nyquist criteria, i.e. $\lambda/2$ at the surface of the body. Under this constraint, when a full tomography of the body [32,33] is not feasible with a priori information [34], then statistical tomography allows to characterize heterogeneity scales [35] and to retrieve composition information (for CONSERT see also [36] and [37]). However, it is likely that a combination of higher data volume by utilization of additional passes, allocation of more ground station time, or mission extension, together with any better than worst-case power availability on the lander platform can result in a much better tomographic coverage.

To achieve a good coverage of Didymoon, seven to ten tomography slices need to be collected, with each measurement sequence taking about 10 hours. Those slices must also be sufficiently separated in space. Thus, the spacecraft has to be able to operate at various latitudes relative to Didymoon.

A single acquisition sequence is composed of a sequence of visibility, occultation and again visibility between orbiter and lander. The first visibility period is mandatory for a time synchronization between orbiter and lander platform. The science measurements are performed during the occultation period. The last visibility slot is re served for calibration. The accuracy on the orbiter trajectory reconstruction needs to be typically a few meters, whereas the altitude reconstruction accuracy should be in the order of about 5°. The radar link budget constrains the operational distance from the orbiter unit to the lander unit to about 10 km.

Concerning the lander, proper operation of the LFR imposes constraints on the landing site selection (Figure 15 and Figure 16). The acquisition geometry constrained by Didymoon's motion around the main body. Most likely, it is in 1:1 spin-orbit resonance, which means that the side facing the main body is always the same, as with Earth's Moon. With a moving spacecraft on the latitude axis the lander needs to land near to the equator of Didymoon, i.e., between -15° and +15° latitude, in order to achieve alternating visibility and occultation periods. In that case, the orbiter spacecraft will be able to cover a range of latitudes between -25° and +25°. This alternation also constrains the longitude of the landing site to a zone between -120° and +120°, with optimal science return between -60° and +60°. It is also constrained by the lander platform's solar energy availability, which means having to avoid eclipses by the main body, and having a "forbidden zone" between -45° and +45° of longitude.
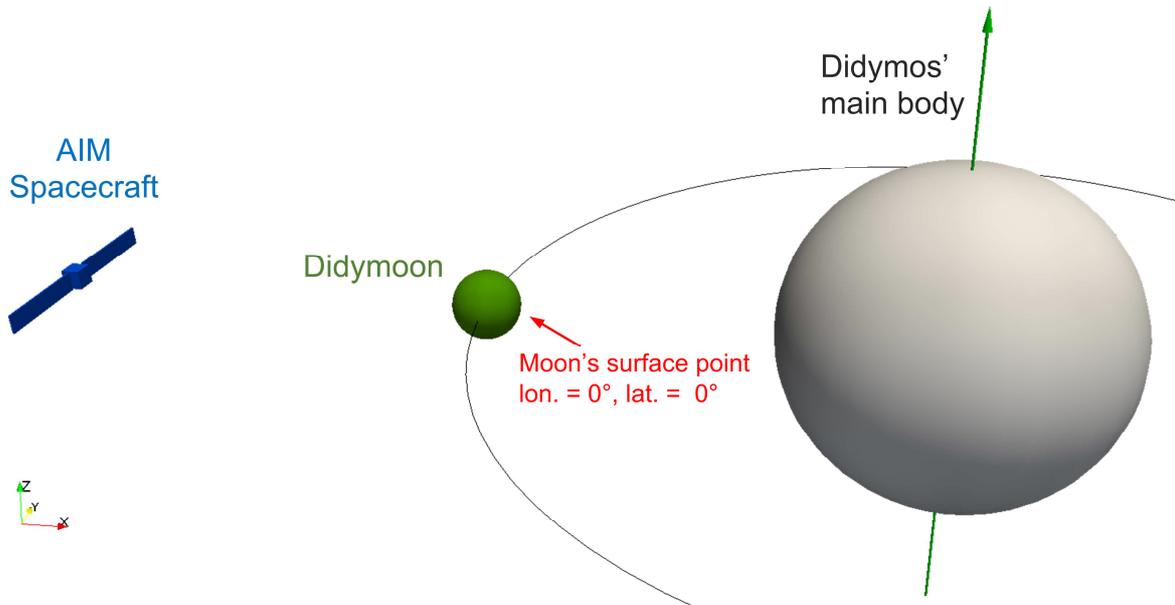
*Figure 15 : Definition of Didymoon reference system.*
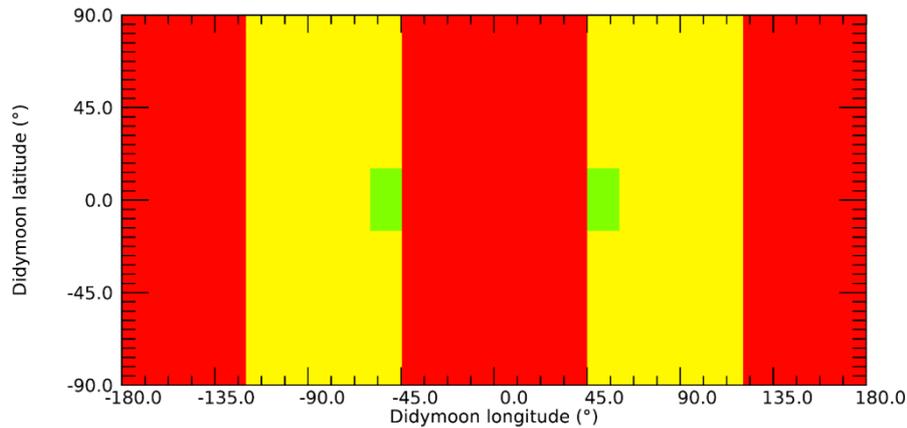
Figure 16: LFR landing site possible areas in green: optimal, yellow: acceptable and red: impossible
0° longitude corresponds to the point facing the main body of the Didymos system.

4.3. Integration into the MASCOT2 Lander Platform

The MASCOT2 lander for the AIM mission is derived from the MASCOT lander, originally designed for and flying on the HAYABUSA2 mission to asteroid (162173) Ryugu [38]. In order to integrate a radar instrument into the lander system, originally envisaged for short lifetime and mobile scouting on an asteroid surface, several changes are incorporated to cope with the measurement and instrument requirements of the radar package. Table 2 shows a summary of the main differences and commonalities between the original MASCOT and the proposed MASCOT2 variant of the lander platform [39,40].

14

Table 2: Main differences and commonalities of the proposed MASCOT2 lander.

Differing attribute	MASCOT	MASCOT2
Main Science Case	surface composition and physical properties mapper	internal structure by radar tomography
Landing site	restricted by thermal and communications reasons	restricted by measurement requirements
Target body diameter	890 m	170 m
Rotation period	7.6 h	11.9 h
Lifetime	˜16 hours	>3 months
Deployment wrt to S/C	sideways, 15° downwards	not restricted
Communications interoperability	synergy with Minerva landers	with AIM ISL (Copins)
Lander mounting plane	15° angled "down"	parallel to the carrier sidewall
Storage	inside panel in a pocket	outside panel, flush
Mobility	1 DOF	2 DOF
Localization	passive, by orbiter	self-localization
Power	primary battery only	solar generator and rechargeable batteries
Thermal Control	variable conductivity	passive (MLI, heater)
Self-awareness	basic	extended sensor suite
Communication	VHF transceiver from JAXA	S-band transceiver
Scientific Payload	MARA, MASCam, MasMAG, MicrOmega	MARA, MASCam, LFR, DACC, (MAG)

The LFR E-Box (Figure 13) is designed in order to be compatible with the MASCOT2 lander platform's available volume. The MASCOT2 lander design is ideally suited to incorporate different suites of payloads, which means that a mechanical integration of the LFR E-Box would have no impact on the overall accommodation. The integration of the LFR's primary antennas and their deployment mechanisms requires a slightly larger effort due to volume restrictions in the bus compartment of the lander

The antenna system is designed to match both, the requirements of the MASCOT2 lander and the influence of surface and subsurface in the vicinity of the lander. EM simulations are used to verify the suitability of the antenna system accommodation. Figure 17 shows a simulation setup and a typical 3D radiation pattern assuming a flat surface. Figure 18 shows the antenna far field diagrams in two planes perpendicular to the surface for 50 MHz, 60MHz and 70MHz.

From an electrical point of view, the integration of the instrument into the lander platform is challenging in two ways: (1) the operational concept along with the overall architecture had to be optimized in order to be compatible with a long-duration high-power measurement mode and (2) precise timing is needed in order to achieve usable instrument characteristics. Both aspects center on the energy demand of the LFR instrument and related services which are based on the need to support a lot of repeated long continuous runs. In contrast, MASCOT aboard HAYABUSA2 is designed to fulfil a short-duration scouting mission. It is expected to operate only on two consecutive asteroid days of ~7.6 h, each.

15
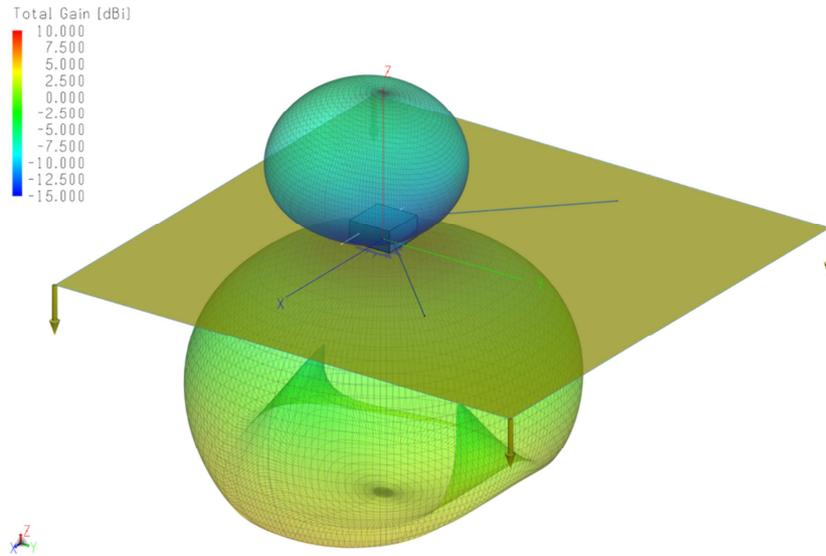
Figure 17: Simulated 3D LFR radiation pattern inside (lower hemisphere) and outside (upper hemisphere) the asteroid at 60 MHz in case of a flat surface, assuming a relative permittivity of 5.
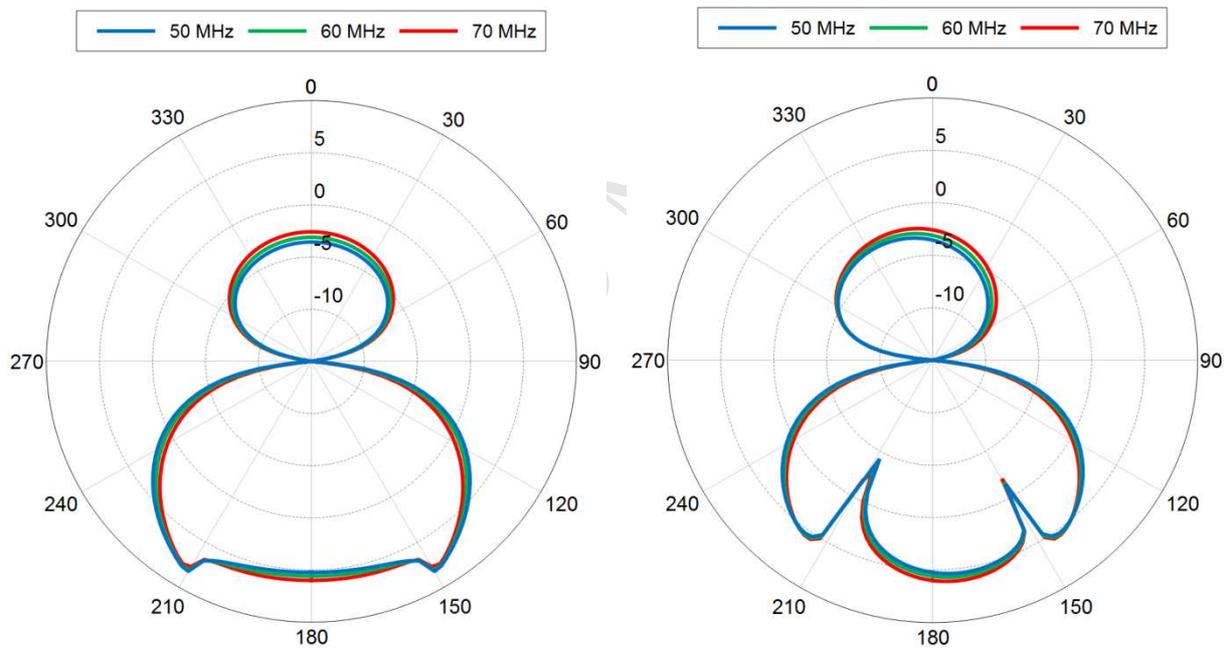

Figure 18: Simulated antenna patterns of MASCOT2 antenna system above ground.
Left: Φ=0° (perpendicular to the y-axis); right: Φ=90° (perpendicular to the x-axis).

The design-driving power consumption results from the operations of the MicrOmega instrument (~20 W total battery power for only ~½ hr) and the mobility unit (up to ~40 W for less than 1.5 s). The energy for this mission is completely provided by a non-rechargeable battery. The choice for primary batteries was partly driven by the fact that such, a power system operates independent of the topographic illumination [41]. A short mission duration also implies few opportunities and little time for ground-loop intervention, thus the power subsystem operates permanently hot-redundant and provides many automatic functions. This leads to an elevated idle power consumption of about 6.5 W, rising to about 10 W with the continuous activity

16

of the MARA and MasMAG instruments. The simplicity of this concept comes at the expense of a very significant thermal design and control effort, required to keep the primary battery cold during interplanetary cruise in order to prevent self-discharge, and warm during on-asteroid operation to ensure maximum use of the available capacity.
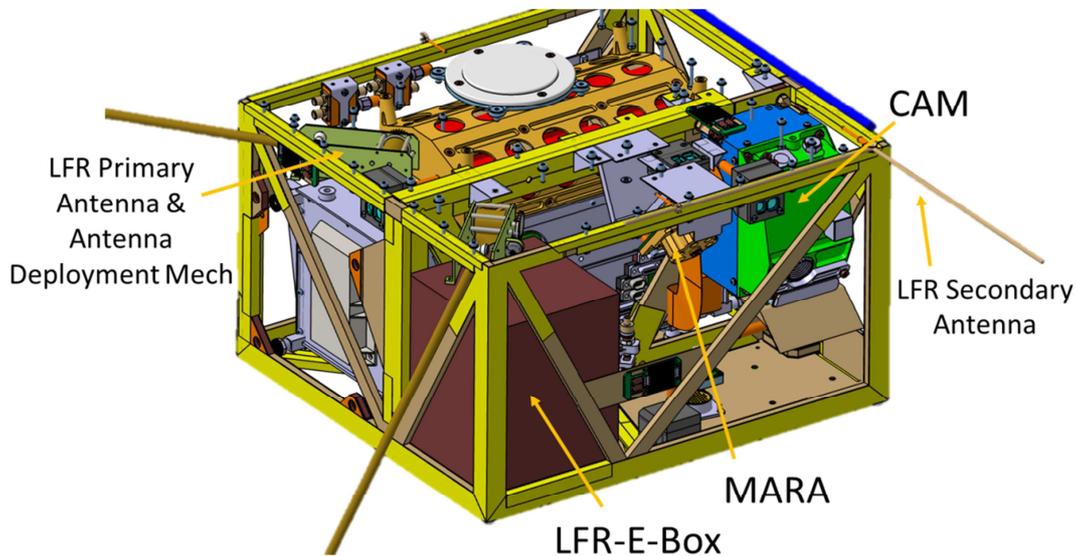
Figure 19: Detailed view of MASCOT2 platform showing accommodation of LFR, including E-box and antenna systems.

This simplicity of the original MASCOT concept comes at the expense of a very significant thermal design and control effort, required to keep the primary battery cold during interplanetary cruise in order to prevent self-discharge, and warm during on-asteroid operation to ensure maximum use of the available capacity. The support of the LFR with its long-duration high-power measurement mode requires modifications to the platform design due to thermal aspects.

The MicrOmega (MMEGA, [42]) instrument, accommodated at the respective location in the original MASCOT lander, requires cold operation due to its infrared sensor and optics. The LFR E-Box can operate in the typical "warm" conditions of other electronics modules (Figure 19). Therefore, its mass can be used together with the bus E-Box and mobility mechanisms to augment thermal energy storage around the battery, improving the mass to surface ratio of the warm compartment and saving electrical energy which would otherwise be required for heating. For this purpose, the cold compartment on the payload side of the lander was reduced to a "cold corner" or pocket around the camera, MasCAM [43], and the radiometer, MARA [44]. The accommodation of the magnetometer, MasMAG [45], as on MASCOT was considered for optional use together with the proposed magnetometer experiments aboard COPINS, sub-satellites to be inserted into orbit in the Didymos system by the AIM spacecraft [46]. A triaxial accelerometer, DACC, was added in order to observe the interaction of the lander with the surface regolith during touch-down, bouncing and self-righting, reaction to motion during deployment operations, and possibly the DART impact shock wave.

For the long-duration MASCOT2 mission, the mission energy demand will be orders of magnitude higher due to the repeated long continuous LFR runs. Thus, a rechargeable battery and photovoltaic power is required. The design-driving power consumption results from the LFR instrument operating for several hours at a time (see Table 1) defining the minimum battery capacity, and the simultaneous operation of the dual mobility mechanism. Both have a similar peak power demand, defining the power handling capability.

A deployable photovoltaic panel is necessary to satisfy the energy demand of LFR operations without too extensive recharging periods between LFR sounding passes. The panel will be released after the MASCOT2 lander relocates to the optimal LFR operations site on Didymoon, self-righted there, and deployed the LFR antennas. The possibility to recharge the battery and wait for ground loop intervention allows mainly cold-redundant operations and reduces the need for highly sophisticated autonomy within the power subsystem. This alone greatly reduces idle power consumption, and thus battery capacity requirements to survive the night. Further reduction of idle consumption is achieved by optimizing the electronics design.

However, the energy demand of LFR is such that a much deeper discharge of the battery will occur as would usually be accepted for Earth-orbiting spacecraft. This will reduce battery lifetime. Thus, some fundamental autonomous functions are used to protect the system from damage by short circuits or deep discharge of the battery and to ensure a restart after the battery has accumulated sufficient energy. For this purpose, the photovoltaic power conversion section charging the battery is self-supplied and does not require battery power to start up. In case the battery gets close to the minimum charge level e.g. when a LFR run cannot be properly terminated due to an unforeseen event, all loads are disconnected so that all incoming photovoltaic power can be used for recharge. State of the art rechargeable batteries can operate sufficiently well and with only minor operational restrictions at cell temperatures from about -20°C to +50°C, nearly as wide as the temperature range of the primary battery of MASCOT, but with much better performance in cold conditions below +20°C. In case the temperature is too low to allow maximum charging rate, all excess photovoltaic power is diverted to a battery heater [47]. During use and in favorable illumination on the ground, battery life extending charge control is applied [48].

As described the features of a long-lived high energy mission can be coped with by a deployable photovoltaic panel. As an alternative a moderate enlargement of the MASCOT-like box shape was also considered as an option for the AIM mission. It could provide the same daily average power level. Depending on which sides of the lander are enlarged, the immediately available photovoltaic power can be adjusted within the daily cycle. A flat shape with a similar top plate area as the deployed panel of MASCOT2 increases power generation around noon while higher or wider sides increase power at sunrise and sunset (assuming a clear view to the horizon at the landing site).
The increased volume, if provided by the carrier mission, can be used to accommodate additional instruments or a larger battery, also providing more robustness during the relocation phases. Depending on the antenna design, relocation for more extensive LFR tomography also becomes possible. It is thus possible to combine investigations of the interior and the surface mineralogy as

carried out by MASCOT. The mass increase is little more than the instrument's, i.e. the bus mass would increase by about 10% with the addition of one relatively large instrument. If the carrier mission provides still more mass allowance, a set of multiple MASCOT type landers based on a common infrastructure but carrying different instruments and individually optimized for these can also be considered [49].

4.4. Design Methodologies for Lander Design Reuse

The "mother" mission of MASCOT, the HAYABUSA2 mission, has benefited greatly from its predecessor HAYABUSA. It reused main portions of the design and optimized its main weaknesses based on lessons learned, such as the antenna, the orientation control and engine as well as the sampling approach [50]. Other than this particular example, and except for the well-known and documented reuse of the Mars Express Flight Spare Hardware for the Venus Express mission [51,52], the MASCOT2 re-use exercise is the only known system level reuse of a previously flown deep space system in a new environment and with an almost completely new science case, as described above. The fostered and maximized re-use of an already very precisely defined system for a very different mission recreates the unusual situation of an extremely wide range of subsystem maturity levels, from concepts to already flown designs. The integration of new instruments like the LFR radar is one of such lower-maturity cases. New design methodologies based on Concurrent Engineering and Model Based Systems Engineering methods can enhance the redesign, instrument integration and system adaptation process and make it faster and more cost efficient [53-55]. In addition, the general use case of a small landing package piggy-backing on a larger main mission is very lucrative and widely applicable in the context of planetary defense and small body exploration, making the platform approach, already known from Earth orbiting missions, a feasible strategy. A strategically planned MASCOT-type lander platform with an ever-increasing portfolio of technology options will further enhance the applicability of the small lander concept to all kinds of missions. Several of the technologies specifically required to realize the radar mission scenario as described above fall into this category. Other technologies such as advanced landing subsystems and new mobility concepts are also interesting and currently under development [56].

5. Conclusions

Direct measurements are mandatory to get a deeper knowledge of the interior structure of NEOs. A radar package consisting of a monostatic high frequency radar and a bistatic low frequency radar is able to perform these direct measurements. Both radar systems provide a strong scientific return by the characterization of asteroid's internal structure and heterogeneity. Whereas the LFR provides a tomography of the deep interior structure, the HFR maps the shallow subsurface layering and connects the surface measurements to the internal structure. In addition to this main objective, the radars can support other instruments providing complementary data sets.

The nanolander MASCOT2 demonstrates, by carrying the mobile part of the bistatic radar, its flexibility. It can carry instruments with a wide range of maturity levels using state of the art design methodologies. As shown, a moderate redesign allows for long-term radar runs in contrast to the original short-term operation scenario of MASCOT.

The presented radar package and the MASCOT2 lander have been developed at phase A/B1 level in the frame of ESA´s AIM mission study. Although the mission has not been confirmed and the next steps to establish such a mission are not clear. The modification of the MASCOT lander platform to a fixed but longtime radar surface station demonstrates the large range of applications for small landing packages on small airless bodies [57]. The radar instrument package presented has a high maturity and is of main interest for planetary defense as well as for NEO science.

References

[1]   A. Herique, et al., Direct Observations of Asteroid Interior and Regolith Structure: Science Measurement Requirements, Advances in Space Research (in press) (2017). doi:10.1016/j.asr.2017.10.020.

[2]   A. Herique, et al., A direct observation of the asteroid's structure from deep interior to regolith: why and how?, in: IAA Planetary Defense Conference, Vol. 4, 2015, paper IAA-PDC-15-04-06.

[3]   A. Herique, V. Ciarletti, A Direct Observation of the Asteroid's Structure from Deep Interior to Regolith: Two Radars on the AIM Mission, in: Lunar and Planetary Science Conference, T315: Planetary Mission Concepts: small Bodies, Vol. 47, The Woodlands, Texas, United States, 2016, pp. 2096.

[4]   P. C. Thomas, J. A. Burns, M. S. Tiscareno, M. M. Hedman, P. Helfenstein, Saturn's Mysterious Arc-Embedded Moons: Recycled Fluff?, in: Lunar and Planetary Science Conference, Vol. 44, 2013, p 1598.

[5]   D. Polishook, N. Moskovitz, A. Thirouin, A. Bosh, S. Levine, C. Zuluaga, S. Tegler, O. Aharonson, The fast spin of near-Earth asteroid (455213) 2001 OE84, revisited after 14 years: constraints on internal structure, Icarus 297 (2017) 126-133. doi:10.1016/j.icarus.2017.06.036

[6]   S. Naidu, L. Benner, M. Brozovic, J.D. Giorgini, M. Busch, J. Jao, C. Lee, L. Snedeker, M. Silva, M. Slade, K. Lawrence, Goldstone radar images of near-Earth asteroids (469896) 2007 WV4, 2014 JO25, 2017 6, and 2017 CS, in: AGU Fall Meeting, December, 2017, New Orleans, USA.

[7]   D. Rubincam, Radiative Spin-up and Spin-down of Small Asteroids, Icarus 148 (1) (2000) 2–11. doi:10.1006/icar.2000.6485.

[8]   S. Jacobson, D. Scheeres, Dynamics of rotationally fissioned asteroids: Source of observed small asteroid systems, Icarus 214 (1) (2011) 161–178. doi:10.1016/j.icarus.2011.04.009.

[9]   S. Ostro, J. Margot, L. Benner, J. Giorgini, D. Scheeres, E. Fahnestock, S. Broschart, J. Bellerose, M. Nolan, C. Magri, P. Pravec, P. Scheirich, R. Rose, R. Jurgens, E. De Jong, S. Suzuki, Radar Imaging of Binary Near-Earth Asteroid (66391) 1999 KW 4, Science 314 (2006) 1276-1280. doi:10.1126/science.1133622.

[10]   P. Michel, et al., Science case for the asteroid impact mission (AIM): A component of the asteroid impact & deflection assessment (AIDA) mission, Advances in Space Research 57 (12) (2016) 2529-2547. doi:10.1016/j.asr.2016.03.031.

[11]   A. F. Cheng, et al., Asteroid impact and deflection assessment mission, Acta Astronautica 115 (2015) 262-269. doi:10.1016/j.actaastro.2015.05.021.

[12]   M. W. Busch et al., Radar observations and the shape of Near-Earth Asteroid 2008 EV5, Icarus 212 (2) (2011) 649-660. doi: 10.1016/j.icarus.2011.01.013.

[13]   D. Scheeres et al., The geophysical environment of bennu, Icarus 276 (2016) 116-140. doi:10.1016/j.icarus.2016.04.013.

[14]   M. Brozivić et al, Goldstone and Arecibo radar observations of (99942) apophis in 2012-2013, Icarus 300 (2017) 115-128. doi:10.1016/j.icarus.2017.08.032.

[15]   M. Pätzold, et al, A homogeneous nucleus for comet 67p/Churyumov-Gerasimenko from its gravity field, Nature 530 (7588) (2016) 63-65. doi:10.1038/nature16535.

[16]   W. Kofman et al., Properties of the 67p/Churyumov-Gerasimenko interior revealed by CONSERT radar, Science 349 (6247) (2015). doi:10.1126/science.aab0639.

[17]   J. Biele et al., The landing(s) of Philae and inferences about comet surface mechanical properties, Science 349 (6247) (2015). doi:10.1126/science.aaa9816.

[18]   F. Braga-Ribas, et al., A ring system detected around the Centaur (10199) Chariklo, Nature 508 (7494) (2014) 72-75. doi:10.1038/nature13155.

[19]   J. Giorgini, S. Ostro, L. Benner, P. Chodas, S. Chesley, R. Hudson, M. Nolan, A. Klemola, E. Standish, R. Jurgens, R. Rose, A. Chamberlin, D. Yeomans, J. Margot, Asteroid 1950 DA's Encounter with Earth in 2880: Physical Limits of Collision Probability Prediction, Science 296 (5565) (2002) 132–136. doi:10.1126/science.1068191.

[20]   A. Milani, S.R. Chesley, M.E. Sansaturio, F. Bernardi, G.B. Valsecchi, O. Arratia, Long-term impact risk for (101955) 1999 RQ36, Icarus 203 (2) (2009) 460-471. doi:/10.1016/j.icarus.2009.05.029.

[21]   S. Ulamec, J. Biele., Relevance of Philae and MASCOT in-situ investigations for planetary, In IAA Planetary Defense Conference, Vol. 4, Frascati, Italy, 2015, paper IAA-PDC-15-04-08.

[22]   P. Michel, et al., European component of the AIDA mission to a binary asteroid: Characterization and interpretation of the impact of the DART mission, Advances in Space Research, (2017). doi.org/10.1016/j.asr.2017.12.020.

[23]   D. Plettemeier, V. Ciarletti, S.-E. Hamran, C. Corbel, P. Cais, W.-S. Benedix, K. Wolf, S. Linke, and S. Roddecke, Full polarimetric GPR antenna system aboard the ExoMars rover, in: 2009 IEEE Radar Conference, IEEE, 2009, pp. 1-6. doi:10.1109/radar.2009.4977120.

[24]   V. Ciarletti, C. Corbel, D. Plettemeier, P. Cais, S. Clifford, and S.-E. Hamran, WISDOM GPR Designed for Shallow and High-Resolution Sounding of the Martian Subsurface, Proceedings of the IEEE 99 (5) (2011) 824-836. doi:10.1109/jproc.2010.2100790.

[25]   I. G. Cumming, F. H. Wong, Digital Processing of Synthetic Aperture Radar Data: Algorithms and Implementation, Artech House, Boston, 2005.

[26]   T. Hagfors, D. Campbell, Mapping of planetary surfaces by radar, Proceedings of the IEEE 61 (9) (1973) 1219-1225. doi:10.1109/PROC.1973.9248.

[27]   W. C. Carrara, R. S. Goodman, R. M. Majewski, Spotlight Synthetic Aperture Radar: Signal Processing Algorithms, Artech House, Boston, 1995.

[28]   G. Picardi, et al., Radar soundings of the subsurface of Mars, Science 310 (5756) 1925-1928. doi:10.1126/science.1122165.

[29]   W. Kofman, et al., The Comet Nucleus Sounding Experiment by Radiowave Transmission (CONSERT). A short description of the instrument and of the commissioning stages, Space Science Reviews 128 (1-4) (2007) 413-432. doi:10.1007/s11214-006-9034-9.

[30]   A. Herique, Y. Rogez, O. P. Pasquero, S. Zine, P. Puget, W. Kofman, Philae localization from CONSERT/Rosetta measurement, Planetary and Space Science 117 (2015) 475-484. doi:10.1016/j.pss.2015.08.020

[31]   O. P. Pasquero, A. Herique, W. Kofman, Oversampled Pulse Compression Based on Signal Modeling: Application to CONSERT/Rosetta Radar, IEEE Transactions on Geoscience and Remote Sensing 55 (4) (2017) 2225-2238, doi:10.1109/TGRS.2016.2639449

[32]   J.-P. Barriot, W. Kofman, A. Herique, S. Leblanc, A. Portal, A two dimensional simulation of the CONSERT experiment (Radio tomography of comet Wirtanen), Advances in Space Research 24 (9) (1999) 1127-1138. doi:10.1016/s0273-1177(99)80206-3.

[33] S. Pursiainen, M. Kaasalainen, Detection of anomalies in radio tomography of asteroids: Source count and forward errors, Planetary and Space Science 99 (2014) 36-47. doi:10.1016/j.pss.2014.04.017.

[34] C. Eyraud, et al., Imaging the interior of a comet from bistatic microwave measurements: Case of a scale comet model, Advances in Space Research (2017). doi:10.1016/j.asr.2017.10.012.

[35] A. Herique, W. Kofman, T. Hagfors, G. Caudal, J.-P. Ayanides, A characterization of a comet nucleus interior, Planetary and Space Science 47 (6-7) (1999) 885-904. doi:10.1016/s0032-0633(98)00144-5.

[36] V. Ciarletti, et al., CONSERT constrains the internal structure of 67p at a few meter size scale, Monthly Notices of the Royal Astronomical Society 469 (2) (2017) 805-817. doi:10.1093/mnras/stx3132.

[37] A. Herique, W. Kofman, P. Beck, L. Bonal, I. Buttarazzi, E. Heggy, J. Lasue, A. C. Levasseur-Regourd, E. Quirico, S. Zine, Cosmochemical implications of CONSERT permittivity characterization of 67p/CG, Monthly Notices of the Royal Astronomical Society 462 (5) (2016) -516-532. doi:10.1093/mnras/stx040.

[38] T.-M. Ho, V. Baturkin, C. Grimm, J. T. Grundmann, C. Hobbie, E. Ksenik, C. Lange, K. Sasaki, M. Schlotterer, M. Talapina, N. Termtanasombat, E.Wejmo, L. Witte, M. Wrasmann, G. Wübbels, J. Rößler, C. Ziach, R. Findlay, J. Biele, C. Krause, S. Ulamec, M. Lange, O. Mierheim, R. Lichtenheldt, M. Maier, J. Reill, H.-J. Sedlmayr, P. Bousquet, A. Bellion, O. Bompis, C. Cenac-Morthe, M. Deleuze, S. Fredon, E. Jurado, E. Canalias, R. Jaumann, J.-P. Bibring, K. H. Glassmeier, D. Herčík, M. Grott, L. Celotti, F. Cordero, J. Hendrikse, T. Okada, MASCOT - The Mobile Asteroid Surface Scout Onboard the Hayabusa2 Mission; Space Science Reviews 208 (1-4) (2016) 339-374. doi:10.1007/s11214-016-0251-6.

[39] C. Lange, et al., MASCOT2 - A Small Body Lander to Investigate the Interior of 65803 Didymos' Moon in the Frame of AIDA/AIM, International Astronautical Congress, 2017, paper IAC-17-A3.4B.3. url:http://elib.dlr.de/116822/.

[40] J. Biele, et al., MASCOT2, a Lander to Characterize the Target of an Asteroid Kinetic Impactor Deflection Test Mission, in: IAA Planetary Defense Conference, Vol. 5, Tokyo, Japan, 2017, paper IAA-PDC-17-05-P14.

[41] J.T. Grundmann, J. Biele, R. Findlay, S. Fredon, T.-M. Ho, C. Krause, S. Ulamec, C. Ziach, One Shot to an Asteroid - MASCOT and the Design of an Exclusively Primary Battery Powered Small Spacecraft in Hardware Design Examples and Operational Considerations, in: European Space Power Conference, Vol. 719 of ESA Special Publication (3051) (2014) 66.

[42] C. Pilorget, J.-P. Bibring, NIR reflectance hyperspectral microscopy for planetary science: Application to the MicrOmega instrument, Planetary and Space Science 76 (2013) 42-52. doi:10.1016/j.pss.2012.11.004.

[43]   R. Jaumann, N. Schmitz, A. Koncz, H. Michaelis, S.E. Schroeder, S. Mottola, F. Trauthan, H. Hoffmann, T. Roatsch, D. Jobs, J. Kachlicki, B. Pforte, R. Terzer, M. Tschentscher, S. Weisse, U. Mueller, L. Perez-Prieto, B. Broll, A. Kruselburger, T.-M. Ho, J. Biele, S. Ulamec, C. Krause, M. Grott, J.-P. Bibring, S. Watanabe, S. Sugita, T. Okada, M. Yoshikawa, H. Yabuta, The Camera of the MASCOT Asteroid Lander on Board Hayabusa2; Space Science Reviews 208 (1-4) (2016) 375-400. doi:10.1007/s11214-016-0263-2.

[44]   M. Grott, J. Knollenberg, B. Borgs, F. Hänschke, E. Kessler, J. Helbert, A. Maturilli, N. Müller, The MASCOT Radiometer MARA for the Hayabusa 2 Mission, Space Science Reviews 208 (1-4) (2016) 413-431. doi:10.1007/s11214-016-0272-1.

[45]   D. Herčík, H.-U. Auster, J. Blum, K.-H. Fornaçon, M. Fujimoto, K. Gebauer, C. Güttler, O. Hillenmaier, A. Hördt, E. Liebert, A. Matsuoka, R. Nomura, I. Richter, B. S., Benjamin P. Weiss, K.-H. Glassmeier, The MASCOT Magnetometer; Space Science Reviews 208 (1-4) (2016) 433-449. doi:10.1007/s11214-016-0236-5.

[46]   R. Walker, et al., Cubesat opportunity payload inter-satellite network sensors (COPINS) on the ESA asteroid impact mission (AIM), in: 7th Interplanetary Cubesat Workshop, 2016, url:https://icubesat.org/papers/2016-2/2016-b-1-2/.

[47]   G. Dudley, ExoMars Rover Battery Modelling & Life Tests, NASA Aerospace Battery Workshop, Huntsville, USA, 2010.

[48]   J.S. Neubauer, A. Bennetti, C. Pearson, N. Simmons, C. Reid, M. Manzo, The Effect of Variable End of Charge Battery Management on Small-Cell Batteries, NASA/TM—2007-215044, AIAA–2007–4789

[49]   J.T. Grundmann, W. Bauer, J. Biele, R. Boden, M. Ceriotti, F. Cordero, B. Dachwald, E. Dumont, C.D. Grimm, D. Herčík, T.-M. Ho, R. Jahnke, A.D. Koch, A. Koncz, C. Krause, C. Lange, R. Lichtenheldt, V. Maiwald, T. Mikschl, E. Mikulz, S. Montenegro, I. Pelivan, A. Peloni, D. Quantius, S. Reershemius, T. Renger, J. Riemann, M. Ruffer, K. Sasaki, N. Schmitz, W. Seboldt, P. Seefeldt, P. Spietz, T. Spröwitz, M. Sznajder, S. Tardivel, N. Tóth, E. Wejmo, F. Wolff, C. Ziach, Capabilities of GOSSAMER-1 derived Small Spacecraft Solar Sails carrying MASCOT-derived Nanolanders for In-Situ Surveying of NEAs, Acta Astronautica , Special Issue: Planetary Defence 2017, (5th IAA Planetary Defense Conference, May, 15th-19th, 2017, Tokyo, Japan).

[50]   Y. Tsuda, S. Nakazawa, K. Kushiki, M. Yoshikawa, H. Kuninaka, S. Watanabe, Flight status of robotic asteroid sample return mission HAYABUSA2. Acta Astronautica 127 (2016) 702-709. doi:10.1016/j.actaastro.2016.01.027.

[51]   D. McCoy, Call for Ideas for the Re-Use of the Mars Express Platform - Platform Capabilities, ESA Briefing Presentation: Mars Express Platform Reuse, 2001.

[52]   D. McCoy, T. Siwitza, R. Gouka, The Venus express mission, European Space Agency Bulletin 124, pp. 10-15, 2005.

[53]   C. Lange, J. T. Grundmann, M. Kretzenbacher, P. M. Fischer, Systematic reuse and platforming: Application examples for enhancing reuse with model-based systems engineering methods in space systems development, Concurrent Engineering (2017). doi:10.1177/1063293X17736358.

[54]   C. Lange, T.-M. Ho, and C. Ziach, A model-based systems engineering approach to design generic system platforms and manage system variants applied to mascot follow-on missions, in: Proceedings of the International Astronautical Congress, 2015. url: http://elib.dlr.de/103050/

[55]   A. Braukhane, D. Quantius, V. Maiwald, O. Romberg, Statistics and Evaluation of 30+ Concurrent Engineering Studies at DLR. 5th International Workshop on System & Concurrent Engineering for Space Applications (SECESA), 2012, Lisbon, Portugal. url:http://elib.dlr.de/78119/

[56]   C. Lange, T.-M. Ho, C.D. Grimm, J.T. Grundmann, C. Ziach, R. Lichtenheldt, Exploring Small Bodies: Nanolander and –spacecraft options derived from the Mobile Asteroid Surface Scout, Advances in Space Research (2017).

[57]   S. Ulamec, J. Biele, P.-W. Bousquet, P. Gaudon, K. Geurts, T.-M. Ho, C. Krause, C. Lange, R. Willnecker, L. Witte, Landing on Small Bodies: From the Rosetta Lander to MASCOT and beyond, Acta Astronautica 93 (2014) 460-466. doi:10.1016/j.actaastro.2013.02.007.

- Direct observations of asteroids by radar to understand accretion and evolution.
- The baseline design of two radars is derived from mission science requirements.
- Surface and subsurface maps are provided by a monostatic high frequency radar.
- Deep interior 2D and 3D tomography is provided by a bistatic low frequency radar.
- Aspects of integrating the bistatic radar onto the reusable MASCOT lander platform.